RSC Advances

PAPER

View Article Online
View Journal | View Issue



Cite this: *RSC Adv.*, 2023, **13**, 14554

# Constructing carbon supported copper-based catalysts for efficient $CO_2$ hydrogenation to methanol

Zhong Xie, *[a] Jinpei Hei,[a] Chuan Li,[a] Xiaojie Yin,[a] Fengyi Wu,[a] Lei Cheng[a] and Sugang Meng *[b]

Received 7th March 2023
Accepted 8th May 2023

DOI: 10.1039/d3ra01502e

rsc.li/rsc-advances

An activated carbon-supported Cu/ZnO catalyst (CCZ-AE-ox) was successfully obtained by the ammonia evaporation method for the hydrogenation of carbon dioxide to methanol, and the surface properties of the catalyst post-calcination and reduction were investigated. Activated carbon facilitated the increased dispersion of the loaded metals, which promote the $CO_2$ space-time yield (STY) of methanol and turnover frequency (TOF) on the active sites. Furthermore, the factors affecting the catalyst in the hydrogenation of $CO_2$ to methanol were in-depth investigated. The larger surface area and higher $CO_2$ adsorption capacity are found to make possible the main attributions of the superior activity of the CCZ-AE-ox catalyst.



## 1. Introduction

The atmospheric $CO_2$ in the world has been continuously increasing since the 1950s, and now has doubled from 212 ppm in 1958 to 445 ppm in 2021.[3] In the context of the greenhouse effect of carbon dioxide on global climate change, increasing attention has been paid to the study of carbon dioxide in recent years.[1,2] To solve the environmental problems as well as the impending lack of energy, it is viewed as a promising and efficient approach for sustainable development to convert $CO_2$ into beneficial compounds and petroleum derivatives. The most attractive and promising production is of methanol by using carbon dioxide as a reactant.[4–10] Most of the methanol synthesis methods adopted copper-based catalysts, like Cu/ZnO/$SiO_2$, Cu/ZnO/$Al_2O_3$, Cu/ZnO, Cu/ZnO/$Al_2O_3$/$ZrO_2$, and so forth.[11–15] Cu reduces activation energy for H dissociation, while ZnO plays a role in dramatically improving the catalytic activity of copper-based catalysts, which can decrease the energy barrier of methanol synthesis by impeding the generation of carbon monoxide and accelerating the H spillover.

Researches have shown many problems with copper-based catalysts. For example, copper sintering can lead to low selectivity, low activity, and short lifetime.[16–18] The two main factors claimed that cause copper sintering are low dispersion and water vapor oxidization of copper, which subsequently results in catalyst deactivation. A great many approaches have been used to solve the copper sintering problem. For example, metal oxides have been added to improve copper dispersion.[19] Moreover, several carriers have been modified to develop copper-based catalysts with $Cu^0$ or $Cu^{\xi+}$ sites.[10] Arena *et al.* reported that the carrier effectively controlled the catalyst texture and metal surface exposure, which in turn influenced its adsorption properties.[20] Copper dispersion and reduction of copper-based catalysts have significantly improved recently, but there is little change in the catalytic activity, which is still at a low level.

Furthermore, the most common catalytic supports are graphene, carbon nanotubes (CNTs), and activated carbon (AC) in view of their large surface area, strong thermal stability, and unique structure.[21] In addition, the functionalization of the carbon surface can greatly promote the anchoring of the metal. The hydrophobic nature of carbon effectively ensures excellent stability even in the presence of water. Many cases have demonstrated that carbon-supported catalysts outperformed traditional oxide-supported catalysts. Fan *et al.* declared that reduced graphene oxide (rGO) supporting copper-based catalysts generated a certain surface area, controlling metal surface exposure and catalyst texture, and accordingly influenced adsorption performance.[22] Cu/ZnO catalysts supported on activated carbon have been achieved for hydrogenation to methanol, promoting the dispersion of ZnO and Cu, and low particle agglomeration.[23] Thus, carbon carrier in combination with Cu–ZnO catalysts is expected to result in extremely active and stable catalysts for methanol generation.

This article adopts the ammonia evaporation approach to produce the activated carbon-supported Cu/ZnO (CCZ) catalysts. Owing to the large surface area, AC successfully enhanced

[a]*Engineering Technology Research Center of Preparation and Application of Industrial Ceramics of Anhui Province, School of Chemistry and Material Engineering, Chaohu University, 1 Bantang Road, Chaohu, 238000, P. R. China. E-mail: zhongxie@chu.edu.cn*

[b]*Key Laboratory of Green and Precise Synthetic Chemistry and Applications, Ministry of Education, Huaibei Normal University, Huaibei, Anhui 235000, P. R. China. E-mail: mengsugang@126.com*

the dispersion of the active Cu species. The purpose of this research is to survey and compare the structure and adsorption properties of the calcined and reduced catalysts and investigate catalytic activity with the aid of a fixed-bed reactor.

## 2. Experimental

### 2.1. Catalyst preparation

All reagents are grade chemicals without in-depth purification. To impregnate copper and zinc precursors on activated carbon, the ammonium evaporation method was adopted. First, a solution containing 2.7511 g of $Cu(NO_3)_2 \cdot 3H_2O$ (Macklin, 99%), 1.7169 g of $Zn(NO_3)_2 \cdot 6H_2O$ (Aladdin, 99%), and 40.4251 g of deionized water were mixed in a three-neck flask. Second, 37 g of $NH_3 \cdot H_2O$ solution (Aladdin, 25%) was added into the above-mentioned solution and stirred at room temperature for 10 min until the solution became dark blue. Then, 5 g of activated carbon (Macklin, 8–16 mesh) was added and formed a suspension under vigorous stirring at 80 °C for 5 hours, and then at 50 °C for 20 hours. Lastly, the temperature of the bath was elevated to 80 °C for 7 hours to evaporate the ammonia and deposit the metal species on the AC. The evaporation ended at a pH reduction to 7–8. Then we filtered the resulting suspension and wash the solid repeatedly with deionized water as well as dry it at 90 °C for 24 hours, followed by the calcination of dried samples at 360 °C for 4 hours under $N_2$ to generate the CCZ-AE-ox. Additionally, the catalyst was reduced under a pressure of 2.5 MPa at 75% $H_2/N_2$ (100 ml $min^{-1}$) flow rate at 300 °C for 1 hour, marked as CCZ-AE-re. The activated carbon calcined at the same conditions without adding metal salts was named AC-ox.

### 2.2. Catalyst characterization

This article researched the chemical ingredient of the catalysts with two methods, namely, the aid of X-ray photoelectron spectroscopy (XPS, Thermo Scientific K-Alpha) and X-ray diffraction (XRD, Rigaku D/MAX-2400). To analyze the bulk composition, the article utilized inductively coupled plasma-atomic emission spectroscopy (ICP-OES; Agilent 5110).

Scanning electron microscopy (SEM, Hitachi Regulus 8100) and high-resolution transmission electron microscopy (HRTEM, FEI Talos-F200S) were scanned to characterize the framework and morphology of the catalysts.

The surface area and pore volume of the catalysts were calculated by BET and BJH methods from nitrogen adsorption–desorption isotherms at 77 K determined with a Micromeritics ASAP 2020 Plus HD88 apparatus.

We used the same instruments as for TPR to conduct the $CO_2$ temperature programmed desorption ($CO_2$-TPD) was conducted using the same instrument as for TPR. First, 200 mg of the sample was reduced in inflowing 10% $H_2$/Ar at 300 °C for 30 min, cooled to 50 °C, and exposed to pure CO2 for 1 h, followed by purging with Ar for 1 h to remove the physisorbed molecules. Finally, the TPD measurement was carried out in flowing Ar and heated up to 900 °C with a heating rate of 10 °C $min^{-1}$.

$H_2$ temperature-programmed reduction (TPR) was conducted on a Micromeritics AutoChem II 2920 instrument with thermal conductivity (TCD) to test the reducibility of catalysts. 100 mg of the catalyst was put in the U-shaped quartz reactor and then pretreated by pure Ar flow at 300 °C for half an hour. The temperature was reduced to 40 °C, and then flowed 10% $H_2$ in Ar was through the sample at 40 °C for 15 minutes. Finally, the sample was heated to 800 °C at a boosting rate of 10 °C $min^{-1}$.

$N_2O$ oxidation and $H_2$ titration were successively adopted to determine the surface area of metallic copper ($S_{Cu}$). 100 mg of the sample was pretreatment in 10% $H_2$/Ar flow at 300 °C for one hour, then purged it using He (30 mL $min^{-1}$) for half an hour, followed by cooling to 60 °C. After that, a flow of 10% $N_2O$/He (30 mL $min^{-1}$) gas was fed in the reactor for one, hour and conducted the TPR measurement under a flow of 10% $H_2$/Ar (30 mL $min^{-1}$) to 300 °C at a boosting rate of 10 °C $min^{-1}$.

CuO was reduced in the first TPR:

$$CuO + H_2 \rightarrow Cu + H_2O, \text{ hydrogen consumption} = X$$

Reduction of surface copper atoms only:

$$Cu_2O + H_2 \rightarrow 2Cu + H_2O, \text{ hydrogen consumption in this TPR} = Y$$

We calculated the dispersion of Cu ($D$) and exposed Cu surface area ($S$) as follows:

$$D = \frac{2Y}{X} \times 100\%$$

$$S = \frac{2Y \times X}{X \times M_{Cu} \times SD_{Cu}}$$

where $N_A$ denotes number of Avogadro ($6.02 \times 10^{23}$ atoms per mol), $M_{Cu}$ denotes relative atomic mass (63.546 g $mol^{-1}$), and $SD_{Cu}$ denotes quantity of copper atoms per square meter ($1.47 \times 10^{19}$ atoms per m).

### 2.3. Activity test and product analysis

The activity test for $CO_2$ hydrogenation to methanol was performed in a high-pressure fixed-bed stainless steel reactor. 2.841 g of catalyst was placed in the reactor with a quantity of quartz sand on both sides, then reduced the catalyst with 75% $H_2/N_2$ at 300 °C for 1 h under 2.5 MPa pressure, designated as CCZ-AE-re. After the reduction treatment, the temperature of the reactor was cooled to reaction temperature, then a mixed gas of $CO_2/H_2$ was introduced, a gaseous hourly space velocity (GHSV) of 1650–4000 ml $g_{cat}^{-1}$ $h^{-1}$, the temperature from 230 to 280 °C, and the ratio of $H_2/CO_2$ at 0.9–4.1. After the reaction system was stabilized, the liquid products were condensed and analyzed by a gas chromatograph (Huifen 7990) equipped with a flame ionization detector (FID) and a 60 m DB-WAX capillary column. The flow velocity of outlet gas was measured by wet gas

meters, and the composition of the effluent gaseous products was analyzed using gas chromatography with a thermal conductivity detector.

This article defines $CO_2$ conversion, $CH_3OH$ selectivity, space-time yield (STY) of methanol and turnover frequency (TOF) as follows:

$$X_{CO_2}(\%) = \frac{n(CO_2)_{in} - n(CO_2)_{out}}{n(CO_2)_{in}}$$

$$S_{product}(\%) = \frac{n(product)_{out}}{n(CO)_{out} + n(CH_3OH)_{out}}$$

$$STY_{methanol}\left(g_{CH_3OH}\ kg_{cat}^{-1}\ h^{-1}\right) = \frac{F_{CO_2,in} \times X_{CO_2} \times S_{CH_3OH} \times M_{CH_3OH} \times 1000}{W_{cat}}$$

$$TOF_{Cu}\left(s^{-1}\right) = \frac{STY \times M_{Cu} \times 1000}{3600 \times (D_{Cu} \times 0.01) \times X_{CO_2}}$$

where $n$ refers to the molar amount of the molecule in the effluent, $F$ stands for the molar flow rate, $M$ is the molar mass, $D_{Cu}$ indicates the dispersion of Cu and $W$ expresses the weight of the catalyst.

## 3. Results and discussion

### 3.1. The structural and morphological properties

The bulk concentration of Cu and Zn measured by ICP are shown in Table 1. There were 12.12% Cu and 4.43% Zn in the high-temperature calcined CCZ-AE-ox catalyst, the Cu/Zn ratio was 2.82; the copper and zinc content in CCZ-AE-re produced by $H_2/N_2$ reduction of CCZ-AE-ox was decreased to 7.32% and 2.61%, respectively, but Cu/Zn ratio has not changed basically. The unstable particles on the surface of the catalyst were blown away during the reduction process. The invariable Cu/Zn ratio indicated that uniform copper-zinc sediments were generated. Furthermore, the metal has not been detected in AC-ox, showing that all metals in CCZ-AE-ox and CCZ-AE-re were derived from metal salt.

Fig. 1 shows the X-ray diffraction patterns of the catalysts. After being calcinated at 360 °C, the diffraction peaks appeared at 35.4 and 38.9° indexed to the diffractions from lattice planes (002) and (200), which confirmed the monoclinic structure of CuO (PDF# 48-1548). Unique diffraction peaks of ZnO (PDF# 80-0075) appeared at 31.7°, 34.4°, 36.2°, and 47.5° that indexed to (100), (002), (101), and (102). Followed by the reduction process

Table 1 ICP metal loading of the catalysts

| Catalyst | Cu wt% | Zn wt% | Cu/Zn |
|---|---|---|---|
| AC-ox | 0.01 | 0 | — |
| CCZ-AE-ox | 12.12 | 4.43 | 2.82 |
| CCZ-AE-re | 7.32 | 2.61 | 2.89 |

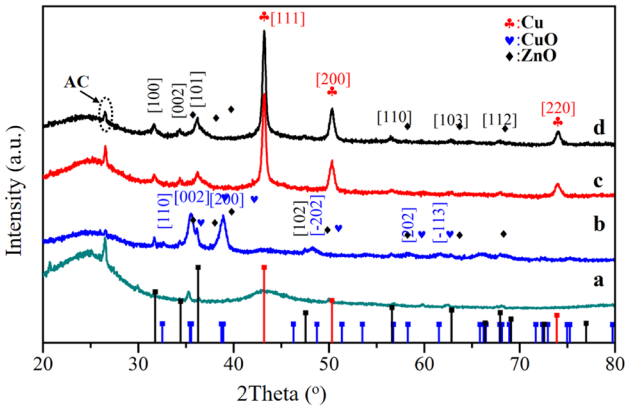


Fig. 1 XRD patterns of the catalysts (a, b, c, and d represent the AC-ox, CCZ-AE-ox, CCZ-AE-re, and spent catalyst, respectively).

at 300 °C, the distinctive peaks of (100), (002), and (110) assigned to ZnO phases showed no obvious changes, while the peaks of CuO phases faded away. The peaks at 43.2°, 50.3°, and 74.9° indexed to (111), (200), and (220) of the metallic Cu, exerting a core effect as an active part in methanol synthesis. Comparing the XRD of the spent catalyst and the fresh catalyst, it can be seen that the catalyst maintained good structural stability.

The results of $N_2$ adsorption–desorption measurements to analyze the physical properties of all catalysts are illustrated in Fig. 2. As seen in Fig. 2A, all isotherms showed obvious microporous adsorption characteristics, demonstrating the existence of narrow micropores. The pore size distributions of the three catalysts exhibited three peaks around 0.7 nm, 1.18 nm, and 1.48 nm in Fig. 2B. Moreover, the surface area (BET) and pore volume ($V_p$) are inserted in Fig. 2A. The $V_p$ of the metal loading catalyst decreased from 0.3794 $cm^3\ g^{-1}$ to 0.2719 $cm^3\ g^{-1}$, indicating numerous Cu and Zn components entered the pores of activated carbon. Nevertheless, when the catalyst of CCZ-AE-ox was reduced, the pore volume of CCZ-AE-re increased to 0.3251 $cm^3\ g^{-1}$. The specific surface area of the catalyst showed similar changes to pore volume. The specific surface of the catalyst fell from 680.5365 m2 $g^{-1}$ to 461.1393 m2 $g^{-1}$ after metal loading and rose to 530.7036 m2 $g^{-1}$ after reduction. The cause possibly lies in two aspects. One was the blockage of the pore of the activated carbon by the loading metal, which resulted in decreased specific surface area of CCZ-AE-ox. Another was the loss of certain metals from the reduced CCZ-AE-re sample, which released the number of pores correspondingly and in turn increased the specific surface area of the catalyst.

The characterizations of scanning electron microscopy (SEM) and elemental mapping analysis were made for investigating the morphology of the catalysts. Seen from SEM images of the CCZ-AE-ox catalyst, the support surface was covered with rough particles (Fig. 3A-1). In the magnification image of Fig. 3A-2 and A-3, it is found that the particles have a lamellar structure. As seen in the element mapping images, he Cu and Zn showed homogeneous distribution in the materials. During the reduction process, the rough packing structure transformed

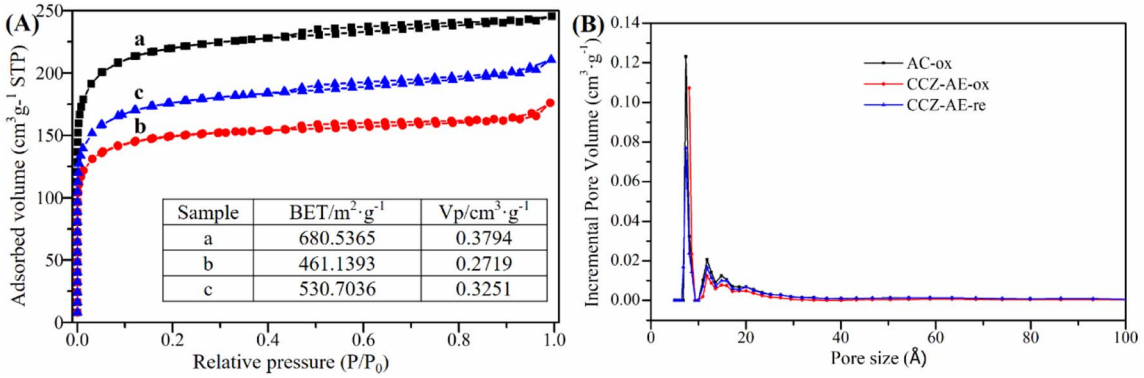


Fig. 2 $N_2$ adsorption–desorption isotherms (A) and pore size distributions (B) of the catalysts (a, b, and c represent AC-ox, CCZ-AE-ox, CCZ-AE-re, respectively).

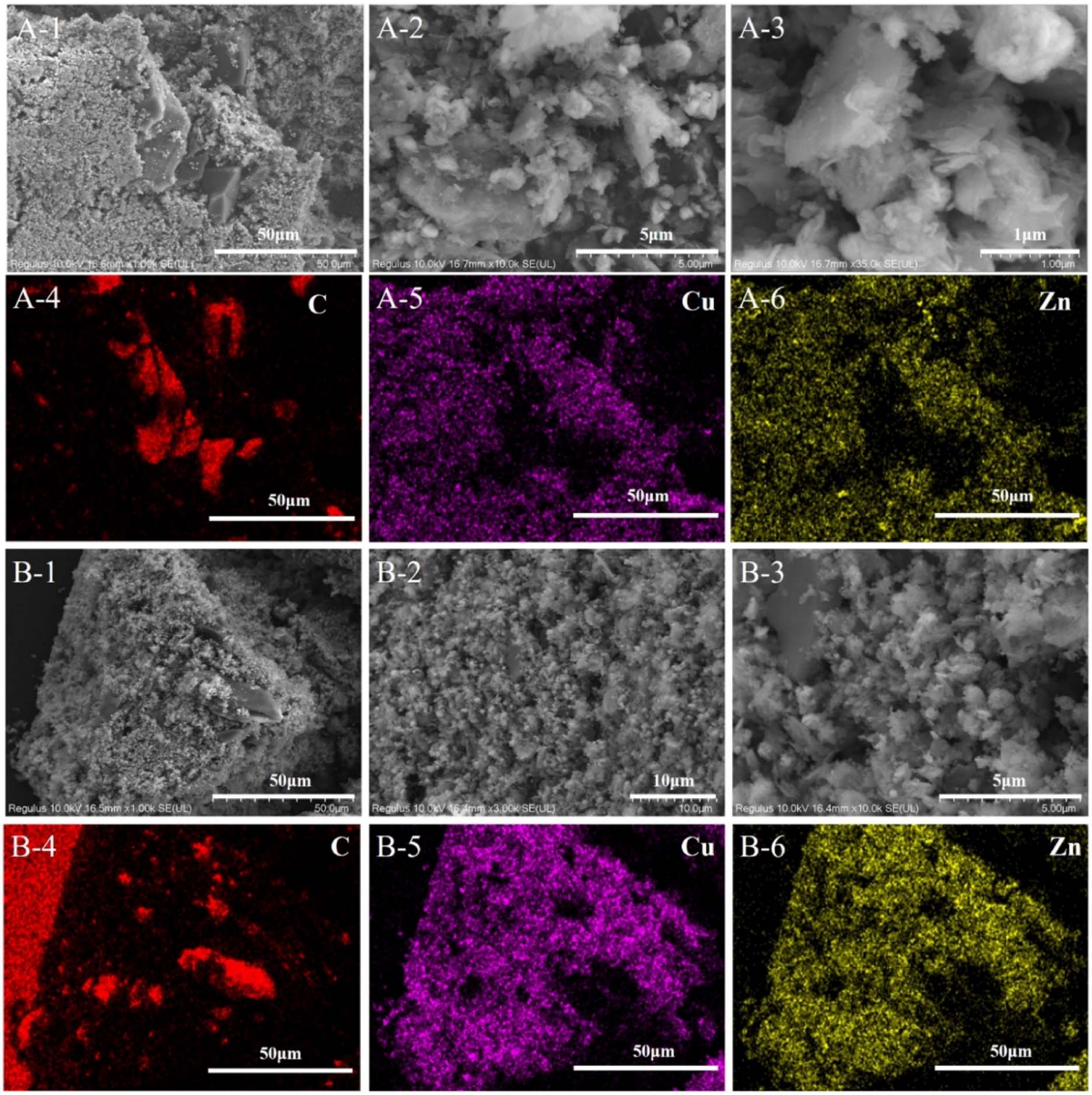


Fig. 3 SEM and element mapping images of CCZ-AE-ox (A), and CCZ-AE-re (B).

into a uniform granular layer, formed by loose spherical particles. The Cu and Zn components were uniformly distributed on the inner surface of the activated carbon.

As seen in Fig. 4A, the TEM images of CCZ-AE-ox showed lattice fringes at 0.231 nm, 0.253 nm, and 0.275 nm ascribed to the characteristic (200), (002) and (110) planes of CuO, respectively. Moreover, the lattice spacings of 0.248 nm and 0.261 nm were also found to be corresponding to ZnO (101) and (002). After being reduced by $H_2$, the CCZ-AE-re catalyst had got prominent lattice stripes of ZnO, displaying new lattice fringe assigned to ZnO (111) but with the disappearance of (101) lattice planes (Fig. 4B). Meanwhile, the lattice spacing of 0.208 nm and 0.181 nm was found to ascribe to Cu (111), (200), which confirmed to the outcomes of XRD. Furthermore, the lattice fringes of $Cu_2O$ (111) emerged in the TEM of the reduced catalyst. As seen from the TEM images, there was a sharp interface between the catalysts and activated carbon, which indicated the active components of the catalyst were well bound to carbon.

### 3.2. Surface composition and reduction behavior

Fig. 5A shows the $CO_2$-TPD curve of different catalysts used in determining the surface basicity, adsorbing, and activating $CO_2$ as well as combining with hydrogen to synthesize methanol. The weak desorption peak of all catalysts occurred at 80–90 °C, ascribing to the physical adsorption of $CO_2$ by activated carbon. No desorption of $CO_2$ occurred in the AC-ox catalyst (the resulting product of the calcination of activated carbon) after 100 °C, thus it's easy to conclude that the adsorption of $CO_2$ on AC-ox was weak. The catalyst of CCZ-AE-ox exhibited a desorption peak at 186 °C, which was assigned to the moderately basic site considered to be metal oxygen pairs (such as Zn–O). By comparison, the desorption temperature of the CCZ-AE-re

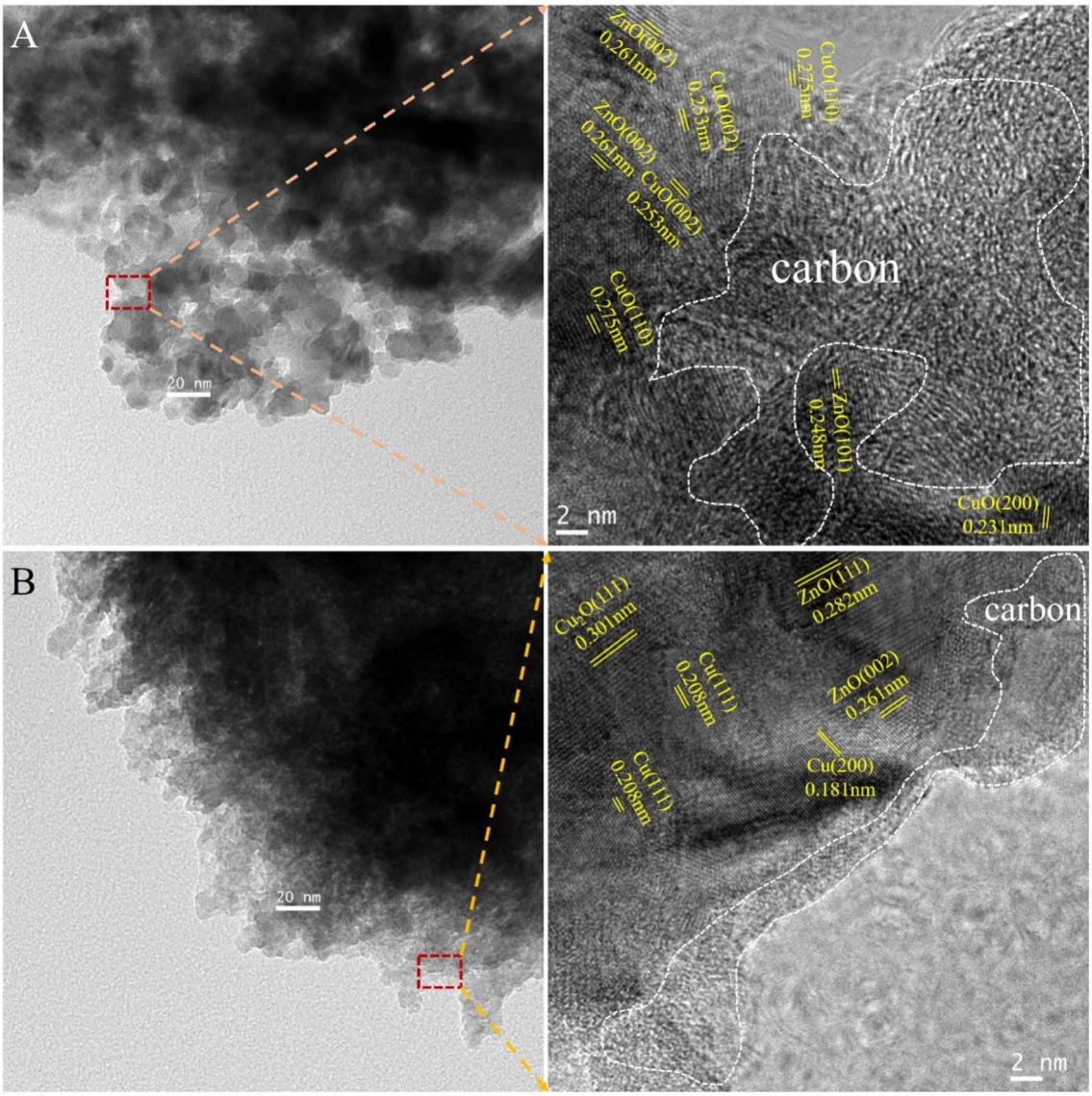


Fig. 4 TEM images of CCZ-AE-ox (A), and CCZ-AE-re (B).

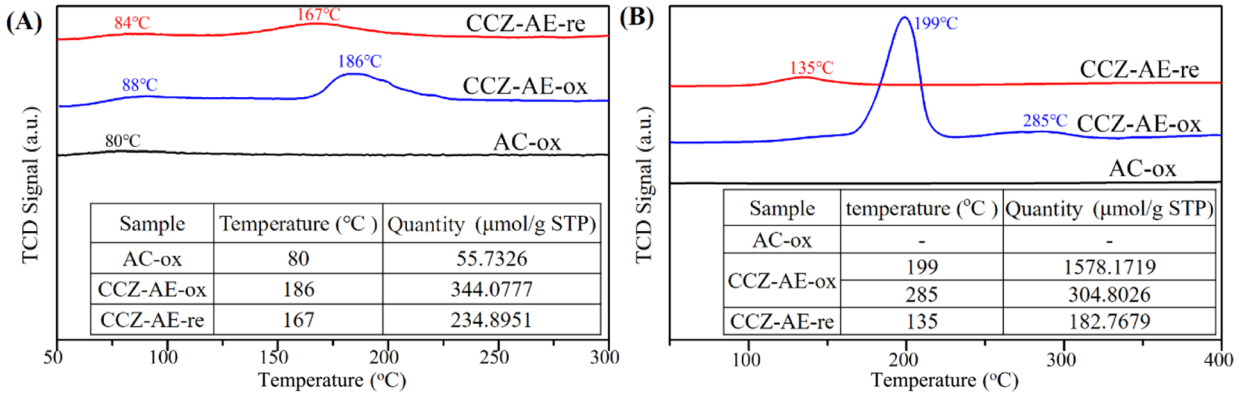


| Sample | Temperature (°C ) | Quantity (μmol/g STP) |
|---|---|---|
| AC-ox | 80 | 55.7326 |
| CCZ-AE-ox | 186 | 344.0777 |
| CCZ-AE-re | 167 | 234.8951 |

| Sample | temperature (°C ) | Quantity (μmol/g STP) |
|---|---|---|
| AC-ox | - | - |
| CCZ-AE-ox | 199 | 1578.1719 |
| | 285 | 304.8026 |
| CCZ-AE-re | 135 | 182.7679 |

Fig. 5 (A) $CO_2$-TPD and (B) $H_2$-TPR profiles of CCZ catalysts.

catalyst was at 167 °C. The slightly lower temperature implied that the basicity of CCZ-AE-re was weakened by the high-pressure reduction of CCZ-AE-ox. Meanwhile, the amounts of $CO_2$ desorbed from the basic site on the two catalysts were quantitatively calculated and summarized (inserted in Fig. 5A). The quantity of $CO_2$ desorbed from CCZ-AE-ox was 344.0777 μmol $g^{-1}$, considerably higher than that of CCZ-AE-re (234.8951 μmol $g^{-1}$), which implied higher pressure for catalyst reduction resulted in less basic sites.

Fig. 5B shows the $H_2$-TPR experiments conducted on three catalysts to study the redox behaviors. No reduction peaks of the calcined activated carbon of AC-ox occurred at 100–400 °C, which implied that AC-ox cannot be reduced at this temperature. For CCZ-AE-ox, the TPR profile features a main peak around 199 °C accompanied by an obvious peak of 285 °C, suggesting a complicated reduction process for CuO species. The peak at 199 °C may be attributed to the reduction of the dispersed $CuO_x$ species.[22,24] In contrast, the higher reduction temperatures at 285 °C, may be ascribed to the reduction of CuO*x* species strongly interacting with the ZnO matrix.[25,26] The peaks in the CCZ-AE-re catalyst located at 135 °C might be attributed to the reduction in the surface $Cu_xO$ species which is oxidized by air oxidation during the test. As shown in the insertion figure of Fig. 5B, the total hydrogen consumption of CCZ-AE-ox was to 1872.97 μmol $g_{cat}^{-1}$, and the calculated Cu content was 11.97%.

Additionally, the metallic Cu dispersion ($D_{Cu}$) and exposed Cu surface area ($S_{Cu}$) catalysts calculated by $N_2O$ chemisorption experiments are important parameters for the activity of Cu-based catalysts for $CO_2$ hydrogenation to methanol. As shown in Table 2, CCZ-AE-ox displays a metal Cu dispersion of 4.14% and Cu surface area of 3.34 $m^2$-Cu per $g_{cat}$. During the high-pressure reduction, the loose particles on the surface of the metal carrier were lost, and the copper-specific surface area of the CCZ-AE-re catalyst fell to 2.74 $m^2$-Cu per $g_{cat}$.

The surface state of the catalyst has a major impact on its catalytic behavior, the elemental chemical state and surface composition of the calcined and reduced catalysts were further evaluated by X-ray photoelectron spectroscopy (XPS) analysis in Fig. 6. Fig. 6A shows the XPS full spectrum of all catalysts, which have shown the peaks of C 1s, O 1s, Cu 2p and Zn 2p. In the C 1s core-level XPS spectrum of Fig. 6B, three peaks occurred in the deconvoluted C 1s spectrum at 284.8, 286.2, and 288.8 eV, corresponding to C atoms in C–C, C–O, and C=O shake-up satellite peak, respectively.[27]

The Cu 2p XPS spectrum is shown in Fig. 5C. The presence of CuO in the CCZ-AE-ox is indicated by the two peaks at 934.4 and 954.2 eV, which correspond to Cu $2p_{3/2}$ and Cu $2p_{1/2}$ of $Cu^{2+}$, respectively.[28–30] Two shake-up peaks occurred at 942.3 and 962.4 eV, which confirmed the presence of $Cu^{2+}$.[31–33] Binding energies centered at 1022.2 and 1045.2 eV derived from $Zn^{2+}$ (Fig. 6D) proved that $Zn^{2+}$ was the existing state of the Zn element.[34] The CCZ-AE-re and spent catalyst occurred two peaks at 932.8 and 952.5 eV, corresponding to Cu $2p_{3/2}$ and Cu $2p_{1/2}$ peaks of $Cu^+/Cu^0$, respectively, which confirmed the presence of low valence copper. Except for the peaks of $Cu^+/Cu^0$, there was another obvious satellite peak, which implied the presence of $Cu^{2+}$ possibly caused by air oxidation during the test.

### 3.3. Catalytic performance for methanol synthesis

To investigate the catalytic performance of samples, we conducted the performance testing of the as-prepared CCZ-AE-ox catalyst for $CO_2$ hydrogenation to methanol. As seen from

Table 2 The results of the dissociative $N_2O$ chemisorption

| Catalyst | $H_2$ consumption, μmol $g_{cat}^{-1}$ | $D_{Cu}$, % | $S_{Cu}$, $m^2$-Cu per $g_{cat}$ | Position, °C |
|---|---|---|---|---|
| CCZ-AC | — | — | — | — |
| CCZ-AE-ox | 39 | 4.14 | 3.34 | 153.7 |
| CCZ-AE-re | 32 | — | 2.74 | 146.3 |

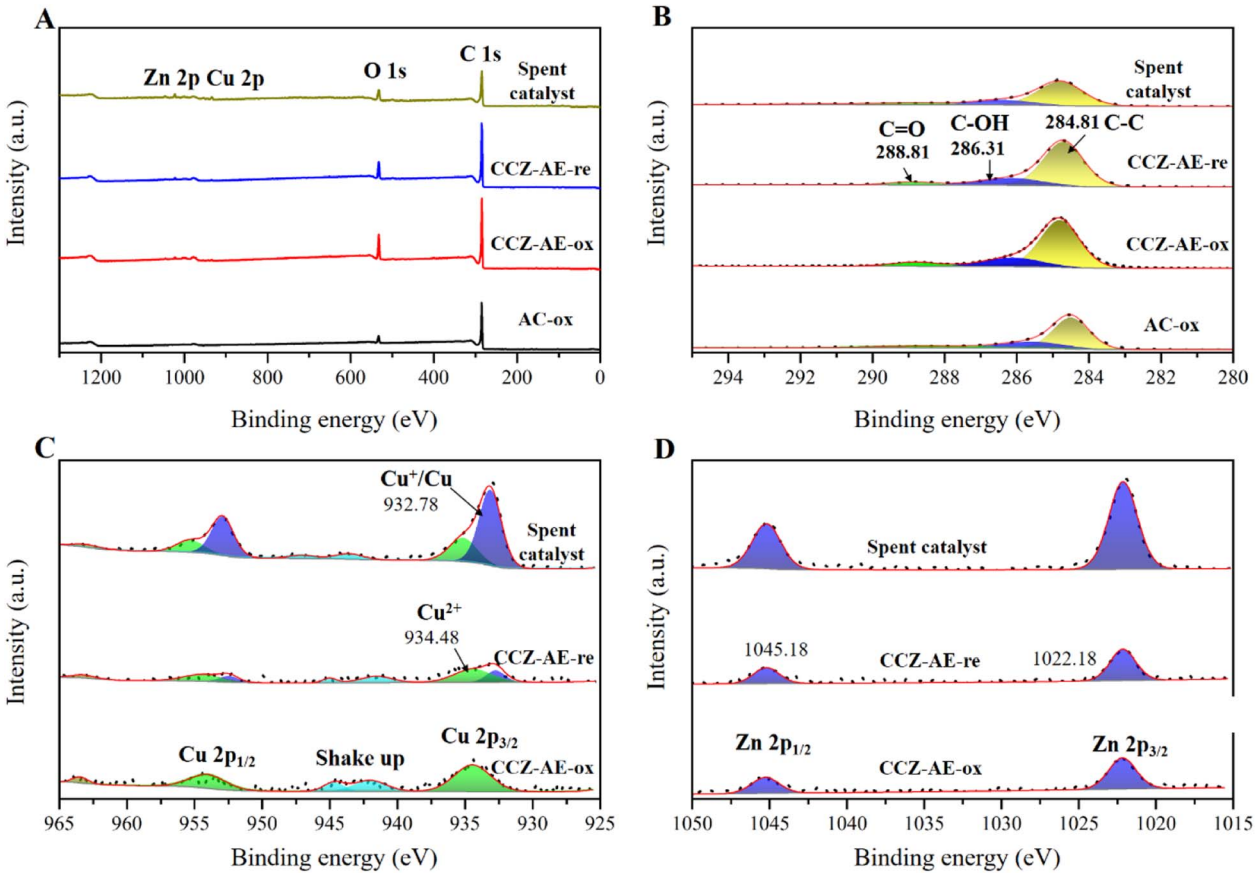


Fig. 6 XPS spectra of the catalyst for (A) full spectra, (B) C 1s, (C) Cu 2p, and (D) Zn 2p.

Fig. 7A and Table 3, the conversion rate of $CO_2$ increased with reaction temperature increasing from 230 °C to 270 °C ($P$ = 2 MPa, GHSV = 3000 $h^{-1}$, $H_2/CO_2$ = 2.4/1), while methanol selectivity showed a downward trend. By contrast, the space-time yield (STY) of $CH_3OH$ increased constantly from 25.75 g $kg_{cat}^{-1}$ $h^{-1}$ to 33.73 g $kg_{cat}^{-1}$ $h^{-1}$. AC-ox was also used as a catalyst for the hydrogenation of carbon dioxide. No apparent $CO_2$ conversion and product generation were found, implying that AC has no catalytic roles.

Increasing the pressure to 2.5 Mpa, the effect of temperature on catalytic performance was like that of 2 MPa, as shown in Fig. 7B. Interestingly, the $CO_2$ conversion and methanol selectivity at 2.5 MPa were both lower than that at 2 MPa under low reaction temperature of 230 °C. However, as the temperature increased, the increasing rate of $CO_2$ conversion was faster than that at 2 Mpa, while the selectivity of methanol decreases more slowly. Finally, at 280 °C, the conversion rate of $CO_2$ reached 14.35% and the selectivity of methanol was only 22.84%. The turnover frequency (TOF), which represents the number of $CO_2$ molecules hydrogenated on a unit site per second ($s^{-1}$), was calculated from the exposed copper surface area for various catalysts. Results from this study (see Table 3) showed that the TOF increased with increased temperature, reaching 6.96 $s^{-1}$ at 270 °C. Further increasing the temperature, the TOF decreased to 4.75 $s^{-1}$ at 280 °C.

The influence of pressure on the performance of CCZ-AE-ox has been shown in Fig. 7C. As the pressure increased from 1.4 MPa to 3.1 MPa, $CO_2$ conversion and TOF inceased from 3.42% and 3.56 × $10^{-3}$ $s^{-1}$ to 5.02% and 5.01 × $10^{-3}$ $s^{-1}$, respectively. The product selectivity remained stable. Increasing the pressure to 4.0 MPa ($T$ = 240 °C; GHSV = 3000 mL $g_{cat}^{-1}$ $h^{-1}$; $H_2/CO_2$ = 2.4/1), the $CO_2$ conversion, $CH_3OH$ selectivity, and TOF showed a downward trend, only the CO selectivity increased from 28.92% to 39.42%. Probably because the pressure affected the gas speed passing through the catalyst bed, so it is necessary to investigate the effect of the gas hourly space velocity (GHSV) on the reaction performance.

As displayed in Fig. 7D, the performance test of CCZ-AE-ox was conducted at 1650–4000 mL $g_{cat}^{-1}$ $h^{-1}$ ($T$ = 250 °C, $P$ = 2.5 MPa, $H_2/CO_2$ = 2.4/1). With the growth of space velocity, the $CO_2$ conversion decreases significantly, but the $CH_3OH$ selectivity tended to increase slightly. In particular, the methanol selectivity remained around 60% in the range of the space velocity from 2100 mL $g_{cat}^{-1}$ $h^{-1}$ to 4000 mL $g_{cat}^{-1}$ $h^{-1}$, and the methanol STY also increased insignificantly, indicating that simply increasing the space velocity to improve the target product was ineffective. This result can be explained that increasing gas space velocity can accelerate the turnover frequency of the activated site of the catalyst, and the TOF increased from 2.82 × $10^{-3}$ $s^{-1}$ at GHSV of 1650 mL $g_{cat}^{-1}$ $h^{-1}$ to

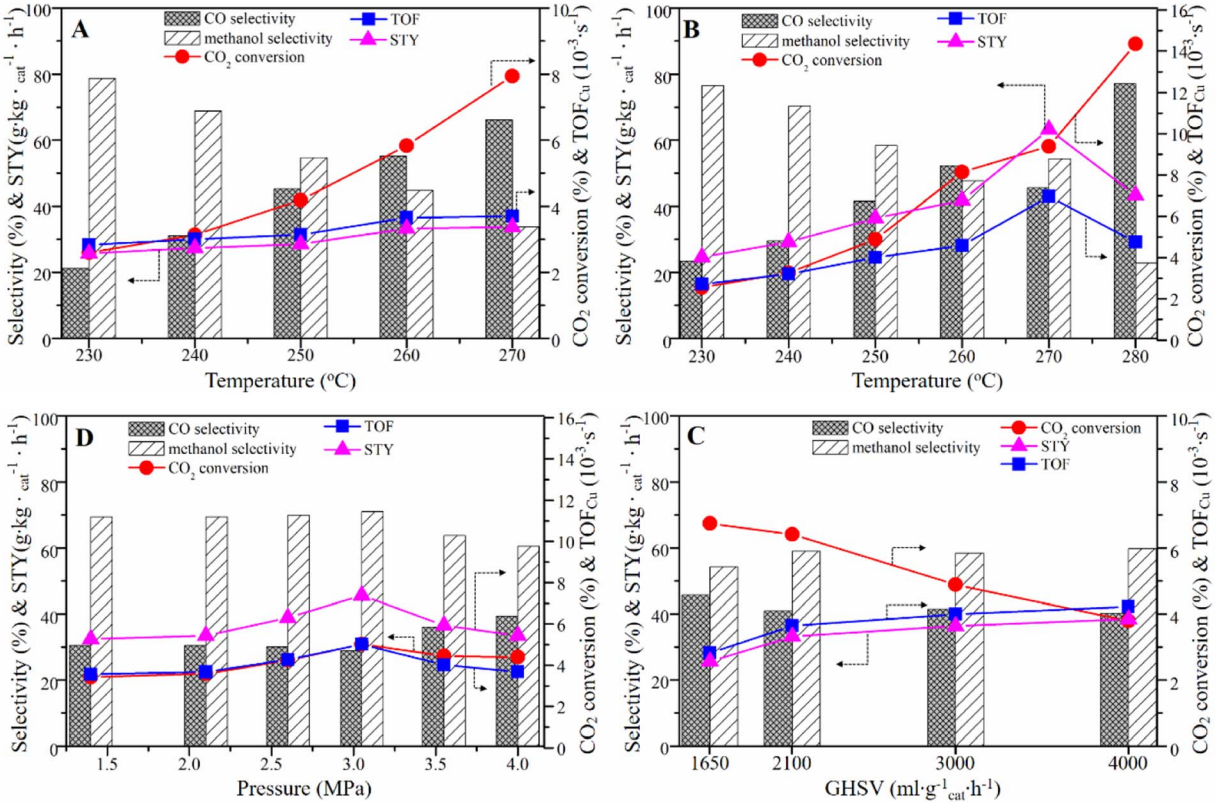


Fig. 7 Catalytic performance of (A) CCZ-AE-ox catalyst at different temperatures with $P = 2$ MPa; and (B) 2.5 MPa (GHSV = 3000 mL $g_{cat}^{-1}$ $h^{-1}$; $H_2/CO_2 = 2.4/1$); (C) CCZ-AE-ox at different pressure ($T = 240$ °C; GHSV = 3000 mL $g_{cat}^{-1}$ $h^{-1}$; $H_2/CO_2 = 2.4/1$), and (D) at various GHSV ($T = 250$ °C; $P = 2.5$ MPa; $H_2/CO_2 = 2.4$).

Table 3 The effect of reaction conditions on the CCZ-AE-ox catalyst

| | | | | | Selectivity/% | | | |
|---|---|---|---|---|---|---|---|---|
| $P$/MPa | $T$/°C | GHSV/$h^{-1}$ | $H_2/CO_2$ | $CO_2$ conversion/% | CO | $CH_3OH$ | STY/g $kg_{cat}^{-1}$ h | TOF/$\times 10^{-3}$ $s^{-1}$ |
| 2 | 230 | 3000 | 2.4 | 2.60 | 21.23 | 21.23 | 78.77 | 25.75 |
| | 240 | | | 3.14 | 31.13 | 31.13 | 68.87 | 27.37 |
| | 250 | | | 4.19 | 45.26 | 45.26 | 54.74 | 28.57 |
| | 260 | | | 5.84 | 55.19 | 55.19 | 44.81 | 33.29 |
| | 270 | | | 7.95 | 66.21 | 66.21 | 33.79 | 33.73 |
| 2.5 | 230 | 3000 | 2.4 | 2.55 | 23.40 | 23.40 | 76.60 | 24.61 |
| | 240 | | | 3.26 | 29.57 | 29.57 | 70.43 | 29.19 |
| | 250 | | | 4.89 | 41.53 | 41.53 | 58.47 | 36.38 |
| | 260 | | | 8.14 | 52.33 | 52.33 | 47.67 | 41.80 |
| | 270 | | | 9.39 | 45.58 | 45.58 | 54.42 | 63.31 |
| | 280 | | | 14.35 | 77.16 | 22.84 | 43.27 | 4.75 |
| 1.4 | 240 | 3000 | 2.4 | 3.42 | 30.50 | 30.50 | 69.50 | 32.40 |
| 2.1 | | | | 3.59 | 30.53 | 30.53 | 69.47 | 33.47 |
| 2.6 | | | | 4.25 | 30.08 | 30.08 | 69.92 | 38.90 |
| 3.1 | | | | 5.02 | 28.92 | 28.92 | 71.08 | 45.64 |
| 3.6 | | | | 4.45 | 36.14 | 36.14 | 63.86 | 36.58 |
| 4.0 | | | | 4.40 | 39.42 | 39.42 | 60.58 | 33.49 |
| 2.5 | 250 | 1650 | 2.4 | 6.75 | 45.70 | 45.70 | 54.30 | 25.67 |
| | | 2100 | | 6.41 | 40.97 | 40.97 | 59.03 | 33.21 |
| | | 3000 | | 4.89 | 41.53 | 41.53 | 58.47 | 36.38 |
| | | 4000 | | 3.80 | 40.24 | 40.24 | 59.76 | 38.46 |
| 2.5 | 250 | 3000 | 0.89 | 2.31 | 61.62 | 61.62 | 38.38 | 20.31 |
| | | | 1.67 | 3.67 | 46.09 | 46.09 | 53.91 | 31.40 |
| | | | 2.39 | 4.89 | 41.53 | 41.53 | 58.47 | 36.39 |
| | | | 3.59 | 6.66 | 38.67 | 38.67 | 61.33 | 36.61 |
| | | | 4.14 | 7.09 | 37.29 | 37.29 | 62.71 | 34.81 |

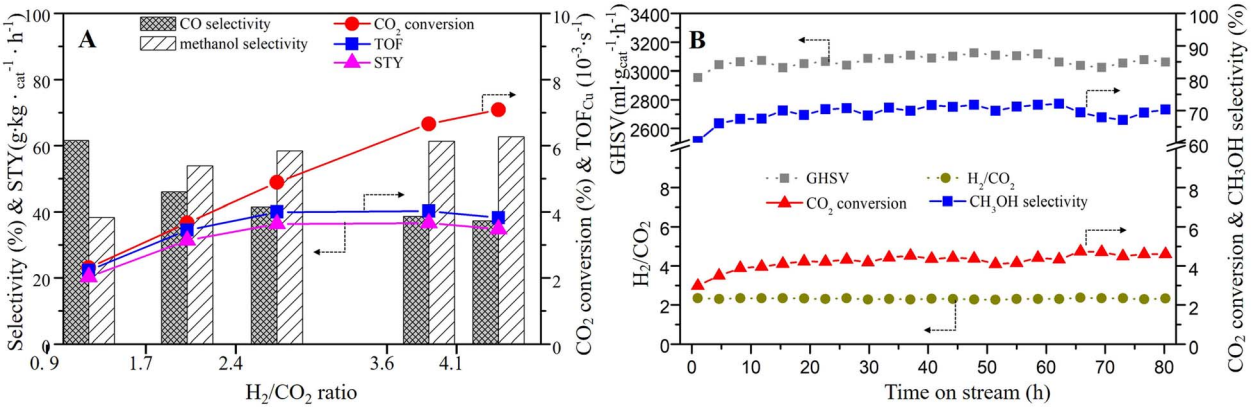


Fig. 8 (A) Effect of $H_2/CO_2$ ratios ($T$ = 250 °C; $P$ = 2.5 MPa; GHSV = 3000 mL $g_{cat}^{-1}$ $h^{-1}$), and (B) the stability test on CCZ-AE-ox catalyst ($T$ = 240 °C; $P$ = 2.5 MPa; GHSV = 3000 mL $g_{cat}^{-1}$ $h^{-1}$).

$4 \times 10^{-3}$ $s^{-1}$ at GHSV of 3000 mL $g_{cat}^{-1}$ $h^{-1}$, but further increasing the GHSV, the TOF did not change obviously.

The influence of the $H_2/CO_2$ ratio on the catalytic performance was also investigated. As can be seen in Fig. 8A and Table 3, with the rise of the $H_2/CO_2$ ratio from 0.9 to 4.1 ($T$ = 250 °C, $P$ = 2.5 MPa, GHSV around 3000 mL $g_{cat}^{-1}$ $h^{-1}$), the $CO_2$ conversion grown significantly from 2.31% to 7.09%. The methanol selectivity also showed an increasing trend, but it was stable when $H_2/CO_2$ ratio reached 3.59. The STY and TOF also increased until the $H_2/CO_2$ ratio reached 3.59.

The stability of the catalyst is an important parameter for hydrogenating $CO_2$ to methanol. The on-stream reaction experiment over CCZ-AE-ox catalyst was carried out under the conditions: $T$ = 240 °C; $P$ = 2.5 MPa; GHSV = 3000 mL $g_{cat}^{-1}$ $h^{-1}$. As shown in Fig. 7B, the $CO_2$ conversion, and $CH_3OH$ selectivity remained almost unchanged after 80 h on stream, which proved that the CCZ-AE-ox catalyst presented stable catalytic performance.

$CO_2$ hydrogenation is the result of the synergistic effect of $CO_2$ and $H_2$. Therefore, a large amount of activated $CO_2$ without sufficient H to react with would desorb from the metal surfaces in the form of $CO_2$ at low $H_2/CO_2$ ratios, resulting in low $CO_2$ conversion and product selectivity. For example, at an $H_2/CO_2$ of 0.9, the methanol selectivity is only 38%. As the increase of $H_2/CO_2$ ratio, more H produced on the $Cu^+/Cu^0$ site will react with $CO_2$, resulting in higher selectivity of methanol. When the activated H exceeds the proportion required for $CO_2$ hydrogenation, the product selectivity will remain stable.

## 4. Conclusions

CCZ-AE-ox catalyst was prepared by ammonia-evaporation method for $CO_2$ hydrogenation to methanol. The introduction of AC improved specific surface CCZ-AE-ox catalyst was prepared by an ammonia-evaporation method for $CO_2$ hydrogenation to methanol. The introduction of an AC support improved the specific surface area of the catalyst. The CCZ-AE-ox catalysts showed only CuO diffraction peaks although activated carbon can provide a reducing atmosphere during the catalyst preparation process. The catalyst CCZ-AE-ox, reduced by $H_2$, showed only the peak of Cu, indicating the complete reduction of CuO to Cu. Meanwhile, in contrast to activated carbon, the $CO_2$ adsorption capacity of the metal-loaded catalyst is significantly higher. The $CO_2$ conversion and $CH_3OH$ selectivity of the CCZ-AE-ox catalyst reached 9.39% and 45.58% under the reaction conditions of 2.5 MPa and 270 °C, while those of the AC-ox catalyst has no obvious catalytic performance. Methanol selectivity increases as the temperature decreases. Increasing temperature, space velocity and $H_2/CO_2$ ratio all improve TOF and STY, but only the methanol selectivity decreases with increasing temperature. The AC support facilitates the production of methanol from $CO_2$ and our catalysts enable high catalytic performance, making full use of the high specific surface area of the activated carbon to achieve better conversion of $CO_2$ at low energy consumption.

## Conflicts of interest

The authors declare that there are no known competing financial interests or personal relationships which have appeared to affect the work reported herein.

## Acknowledgements

This work was supported by the National Natural Science Foundation of China (NSFC, 52002142); The Foundation of Anhui Province for Distinguished Young Scholars (2022AH020038); the Scientific Research Project of Chaohu University (XLY-202005, hxkt20220010, hxkt20220049), and the Start-Up Grant of Chaohu University (KYQD-202003).

## References

1 M. Liu, Y. Yi, L. Wang, H. Guo and A. Bogaerts, Hydrogenation of Carbon Dioxide to Value-Added Chemicals by Heterogeneous Catalysis and Plasma Catalysis, *Catalysts*, 2019, **9**, 275.

2 S. G. Meng, C. Chen, X. Gu, H. Wu, Q. Meng, J. Zhang, S. Chen, X. Fu, D. Liu and W. Lei, Efficient photocatalytic $H_2$ evolution, $CO_2$ reduction and $N_2$ fixation coupled with organic synthesis by cocatalyst and vacancies engineering, *Appl. Catal., B*, 2021, **285**, 119789.

3 R. F. Keeling and C. D. Keeling, *Atmospheric Monthly In Situ $CO_2$ Data*, Mauna Loa Observatory, Hawaii (Archive 2021-09-07). In Scripps CO2 Program Data. UC San Diego Library Digital Collections. Available online: **https://library.ucsd.edu/dc/object/bb3859642r**.

4 B. Liang, J. Ma, X. Su, C. Yang, H. Duan, H. Zhou, S. Deng, L. Li and Y. Huang, Investigation on Deactivation of Cu/ZnO/$Al_2O_3$ Catalyst for $CO_2$ Hydrogenation to Methanol, *Ind. Eng. Chem. Res.*, 2019, **58**, 9030–9037.

5 A. Goeppert, M. Czaun, J. P. Jones, G. K. S. Prakash and G. A. Olah, Recycling of carbon dioxide to methanol and derived products-closing the loop, *Chem. Soc. Rev.*, 2014, **43**, 7995–8048.

6 G. A. Olah, G. K. S. Prakash and A. Goeppert, Anthropogenic Chemical Carbon Cycle for a Sustainable Future, *J. Am. Chem. Soc.*, 2011, **133**, 12881–12898.

7 N. A. M. Razali, K. T. Lee, S. Bhatia and A. R. Mohamed, Heterogeneous catalysts for production of chemicals using carbon dioxide as raw material: A review, *Renewable Sustainable Energy Rev.*, 2012, **16**, 4951–4964.

8 O. Martin, A. J. Martin, C. Mondelli, S. Mitchell, T. F. Segawa, R. Hauert, C. Drouilly, D. Curulla-Ferre and J. Perez-Ramirez, Indium Oxide as a Superior Catalyst for Methanol Synthesis by $CO_2$ Hydrogenation, *Angew. Chem., Int. Ed.*, 2016, **55**, 6261–6265.

9 B. An, J. Z. Zhang, K. Cheng, P. F. Ji, C. Wang and W. B. Lin, Confinement of Ultrasmall Cu/$ZnO_x$ Nanoparticles in Metal–Organic Frameworks for Selective Methanol Synthesis from Catalytic Hydrogenation of $CO_2$, *J. Am. Chem. Soc.*, 2017, **139**, 3834–3840.

10 A. García-Trenco, E. R. White, A. Regoutz, D. J. Payne, M. S. P. Shaffer and C. K. Williams, $Pd_2Ga$-Based Colloids as Highly Active Catalysts for the Hydrogenation of $CO_2$ to Methanol, *ACS Catal.*, 2017, **7**, 1186–1196.

11 Q. Sun, Y. L. Zhang, H. Y. Chen, J. F. Deng, D. Wu and S. Y. Chen, A Novel Process for the Preparation of Cu/ZnO and Cu/ZnO/$Al_2O_3$ Ultrafine Catalyst: Structure, Surface Properties, and Activity for Methanol Synthesis from $CO_2$+$H_2$, *J. Catal.*, 1997, **167**, 92–105.

12 C. Baltes, S. Vukojević and F. Schüth, Correlations between synthesis, precursor, and catalyst structure and activity of a large set of CuO/ZnO/$Al_2O_3$ catalysts for methanol synthesis, *J. Catal.*, 2008, **258**, 334–344.

13 P. Gao, F. Li, H. J. Zhan, N. Zhao, F. K. Xiao, W. Wei, L. S. Zhong, H. Wang and Y. H. Sun, Influence of Zr on the performance of Cu/Zn/Al/Zr catalysts via hydrotalcite-like precursors for $CO_2$ hydrogenation to methanol, *J. Catal.*, 2013, **298**, 51–60.

14 S. Natesakhawat, J. W. Lekse, J. P. Baltrus, P. R. Ohodnicki, B. H. Howard, X. Deng and C. Matranga, Active Sites and Structure-Activity Relationships of Copper-Based Catalysts for Carbon Dioxide Hydrogenation to Methanol, *ACS Catal.*, 2012, **2**, 1667–1676.

15 P. Gao, H. Y. Yang, L. N. Zhang, C. Zhang, L. S. Zhong, H. Wang, W. Wei and Y. H. Sun, Fluorinated Cu/Zn/Al/Zr hydrotalcites derived nanocatalysts for $CO_2$ hydrogenation to methanol, *J. $CO_2$ Util.*, 2016, **16**, 32–41.

16 H. Ahouari, A. Soualah, A. Le Valant, L. Pinard, P. Magnoux and Y. Pouilloux, Methanol synthesis from $CO_2$ hydrogenation over copper based catalysts, *React. Kinet., Mech. Catal.*, 2013, **110**, 131–145.

17 H. Zhan, F. Li, P. Gao, N. Zhao, F. Xiao, W. Wei, L. Zhong and Y. Sun, Methanol synthesis from $CO_2$ hydrogenation over La-M-Cu-Zn-O (M = Y, Ce, Mg, Zr) catalysts derived from perovskite-type precursors, *J. Power Sources*, 2014, **251**, 113–121.

18 X. Guo, D. Mao, G. Lu, S. Wang and G. Wu, Glycine-nitrate combustion synthesis of CuO-ZnO-$ZrO_2$ catalysts for methanol synthesis from $CO_2$ hydrogenation, *J. Catal.*, 2010, **271**, 178–185.

19 E. Samei, M. Taghizadeh and M. Bahmani, Enhancement of stability and activity of Cu/ZnO/$Al_2O_3$ catalysts by colloidal silica and metal oxides additives for methanol synthesis from a $CO_2$-rich feed, *Fuel Process. Technol.*, 2012, **96**, 128–133.

20 F. Arena, G. Mezzatesta, G. Zafarana, G. Trunfio, F. Frusteri and L. Spadaro, Effects of oxide carriers on surface functionality and process performance of the Cu-ZnO system in the methanol synthesis via $CO_2$ hydrogenation, *J. Catal.*, 2013, **300**, 141–151.

21 H. Dai, Y. P. Qiu, H. B. Dai and P. Wang, Ni-Pt/$CeO_2$ Loaded On Granular Activated Carbon: An Efficient Monolithic Catalyst for Controlled Hydrogen Generation From Hydrous Hydrazine, *ACS Sustainable Chem. Eng.*, 2018, **6**, 9876–9882.

22 Y. J. Fan and S. F. Wu, A graphene-supported copper-based catalyst for the hydrogenation of carbon dioxide to form methanol, *J. $CO_2$ Util.*, 2016, **16**, 150–156.

23 Z. Luo, S. S. Tian and Z. Wang, Enhanced Activity of Cu/ZnO/C Catalysts Prepared by Cold Plasma for $CO_2$ Hydrogenation to Methanol, *Ind. Eng. Chem. Res.*, 2020, **59**, 5657–5663.

24 X. Zhang, L. Zhong, Q. Guo, H. Fan, H. Zheng and K. Xie, Influence of the calcination on the activity and stability of the Cu/ZnO/$Al_2O_3$ catalyst in liquid phase methanol synthesis, *Fuel*, 2010, **89**, 1348–1352.

25 Y. Zhu, X. Kong, S. Zhu, F. Dong, H. Zheng, Y. Zhu and Y. Li, Construction of Cu/$ZrO_2$/$Al_2O_3$ composites for ethanol synthesis: synergies of ternary sites for cascade reaction, *Appl. Catal., B*, 2015, **166–167**, 551–559.

26 Y. Jiang, H. Yang, P. Gao, X. Li, J. Zhang, H. Liu, H. Wang, W. Wei and Y. Sun, Slurry methanol synthesis from $CO_2$ hydrogenation over micro-spherical $SiO_2$ support Cu/ZnO catalysts, *J. $CO_2$ Util.*, 2018, **26**, 642–651.

27 N. B. Trung, T. V. Tam, H. R. Kim, S. H. Hur, E. J. Kim and W. M. Choi, Three-Dimensional Hollow Balls of Graphene-Polyaniline Hybrids for Supercapacitor Applications, *Chem. Eng. J.*, 2014, **255**, 89–96.

28 J. Liu, A. Zhang, X. Jiang, M. Liu, Y. Sun, C. Song and X. Guo, Selective $CO_2$ Hydrogenation to Hydrocarbons On Cu-Promoted Fe Based Catalysts: Dependence On Cu-Fe Interaction, *ACS Sustainable Chem. Eng.*, 2018, **6**, 10182–10190.

29 K. Wang, X. Dong, C. Zhao, X. Qian and Y. Xu, Facile Synthesis of $Cu_2O$/CuO/RGO Nanocomposite and its Superior Cyclability in Supercapacitor, *Electrochim. Acta*, 2015, **152**, 433–442.

30 Y. Liu, W. Zong, H. Zhou, D. Wang, R. Cao, J. Zhan, L. Liu and B. W. L. Jang, Tuning the Interlayer Cations of Birnessite-Type $MnO_2$ to Enhance its Oxidation Ability for Gaseous Benzene with Water Resistance, *Catal. Sci. Technol.*, 2018, **8**, 5344–5358.

31 V. Deerattrakul, P. Dittanet, M. Sawangphruk and P. Kongkachuichay, $CO_2$ Hydrogenation to Methanol Using Cu-Zn Catalyst Supported On Reduced Graphene Oxide Nanosheets, *J. $CO_2$ Util.*, 2016, **16**, 104–113.

32 H. Noei, H. S. Qiu, Y. M. Wang, E. Loffler, C. Woll and M. Muhler, The identification of hydroxyl groups on ZnO nanoparticles by infrared spectroscopy, *Phys. Chem. Chem. Phys.*, 2008, **10**, 7092–7097.

33 Y. Wang, M. Muhler and Ch. Woll, Spectroscopic evidence for the partial dissociation of $H_2O$ on ZnO(1010), *Phys. Chem. Chem. Phys.*, 2006, **8**, 1521–1524.

34 X. Hu, W. Qin, Q. Guan and W. Li, The Synergistic Effect of $CuZnCeO_x$ in Controlling the Formation of Methanol and CO from $CO_2$ Hydrogenation, *ChemCatChem*, 2018, **10**, 4438–4449.